Nuclear Data for Science and Technology (1988 MITO), 1129-1136, Copyright © 1988 JAERI.

DEVELOPMENT OF NUCLEAR MODELS FOR HIGHER ENERGY CALCULATIONS

Michael Bozoian, Edward R. Siciliano, and Richard D. Smith

Theoretical Division
Los Alamos National Laboratory
Los Alamos, New Mexico, USA

Abstract: Two nuclear models for higher energy calculations have been developed in the regions of high and low energy transfer, respectively. In the former, a relativistic hybrid-type preequilibrium model is compared with data ranging from 60 to 800 MeV. Also, the GNASH exciton preequilibrium-model code with higher energy improvements is compared with data at 200 and 318 MeV. In the region of low energy transfer, nucleon-nucleus scattering is predominately a direct reaction involving quasi-elastic collisions with one or more target nucleons. We discuss various aspects of quasi-elastic scattering which are important in understanding features of cross sections and spin observables. These include 1) contributions from multi-step processes; 2) damping of the continuum response from 2p-2h excitations; 3) the "optimal" choice of frame in which to evaluate the nucleon-nucleon amplitudes; and 4) the effect of optical and spin-orbit distortions, which are included in a model based on the RPA the DWIA and the eikonal approximation.

(Keywords: high-energy nucleon-nucleus, preequilibrium, quasi-elastic models)

Introduction

High energy nucleon-nucleus scattering provides an excellent tool for probing nuclear structure. It also has many practical applications which are supported by the nuclear data libraries,[1] such as the development of particle accelerators.[2] The need to understand the full energy spectrum has stimulated the development of nuclear models for preequilibrium and quasi-elastic reactions which dominate the spectrum at high excitation. This paper is divided into two parts. The first part describes comparisons of both a relativistic hybrid-type and the GNASH exciton-type preequilibrium models to higher energy data. The second part investigates extentions and corrections to the standard quasi-elastic scattering model based on Glauber theory and the RPA nuclear response function.

The Preequilibrium Region

The Hybrid-Type Model

In this section a hybrid-type preequilibrium model is presented, which differs from that described in the literature [3] by incorporating an intranuclear transition rate based on realistic mean free pathes in nuclear matter, relativistic corrections to the particle emmision rate, a relativistically invariant free scattering kernel for calculating angular-distributed spectra, and correct inclusive-model chaining.

The double differential cross section for the emission of a particle ν with energy ϵ into the solid angle Ω is

$$\frac{d\sigma_\nu}{d\epsilon d\Omega} = \sigma_R \sum_n W_\nu(\epsilon, n)\, Q(n,\Omega)\, D(n) \qquad (1)$$

where σ_R is the reaction cross section, $W_\nu(\epsilon, n)$ is the particle emission rate per MeV, $Q(n,\Omega)$ is the occupation probability for the exciton angular-distributed state (n,Ω), and $D(n)$ is the depletion factor.

The particle emission rate is given by

$$W_\nu(\epsilon, n) = ({}_nX_\nu)\,\rho\,\frac{\lambda_C^R(\epsilon)}{\lambda_C^R(\epsilon) + \lambda^+(\epsilon)} \qquad (2)$$

where ${}_nX_\nu$ is the number of nucleons of type ν in the exciton state n, which satisfies $\sum_\nu({}_nX_\nu) = p$, where p is the number of particles in the exciton state n, and $n = p + h$, where h is the number of hole states. $\rho = \left(1 - \frac{\epsilon+\Delta}{E}\right)^{n-2} \frac{(n-1)}{E}$ is obtained from the William's level-density formula with the incident energy E and separation plus Pauli-exclusion energy Δ for particle ν. The intranuclear particle transition rate λ^+ has been relativistically parameterized to the mean-free paths of protons in nuclei from ^{27}Al to ^{208}Pb in the energy range 40 to 200 MeV [4]

$$\lambda^+(\epsilon) = \frac{c\,\beta}{\lambda_m} \quad (\mathrm{sec}^{-1})$$

$$\beta = \sqrt{1 - \left(\frac{\mu_\nu c^2}{\epsilon + \mu_\nu c^2}\right)^2} \qquad (3)$$

with $c = 3 \cdot 10^{23}$ fm/sec. $\mu_\nu c^2$ is the ν-type nucleon rest energy, and $\lambda_m = (4.94 + 1.6f) - 1.21\exp(-E/60)$ fm, where $f = 1 - A/208$ for $27 \le A \le 208$. Finally, the relativistic emission rate $\lambda_C^R(\epsilon)$ is $(1 + \epsilon/2\mu_\nu c^2)$ times Ericson's expression [5] for the nonrelativistic emmision rate obtained from detailed balance

$$\lambda_c^R(\epsilon) = \left(1 + \frac{\epsilon}{2\mu_\nu c^2}\right)\frac{2s_\nu + 1}{\pi^2\hbar^3}\mu_\nu\,\epsilon\,\sigma_\nu(\epsilon) \qquad (4)$$

with s_ν the spin and $\sigma_\nu(\epsilon)$ the inverse cross section for the ν-type particle.

Expressions for $Q(n,\Omega)$ [6] and $D(n)$ [7] are well established in the literature and have been used in Eq. (1). It can be shown,[8] in the context of the preequilibrium model's use of the free scattering kernel, which forms the basis of $Q(n,\Omega)$, that by using relativistic transformations between three frames of reference, both the the free scattering kernel and its eigenvalue equation are relativistic invariants, and so therefore, is $Q(n,\Omega)$.

Finally, because the hybrid model is an inclusive model in which all p particles in the n^{th} exciton state are capable of intranuclear transitions or emissions, the proper chaining is $n \to 3n$, not $n \to 2n$,[9] and the former has been used in Eq. (1).

Equation (1) is only a preequilibrium model. It contains neither an evaporation nor a Hauser-Feshbach model. The

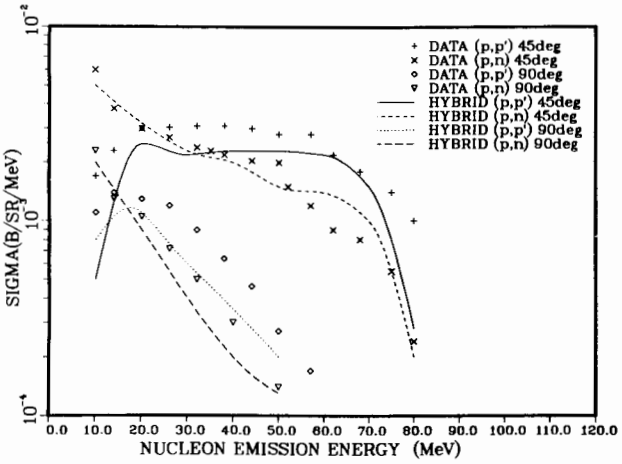

Figure 1: 90 MeV ^{209}Bi(p,p') and ^{209}Bi(p,n) at 45° and 90°.

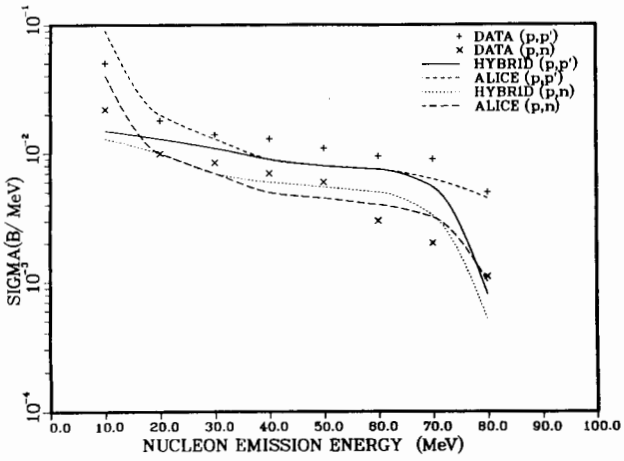

Figure 2: 90 MeV ^{90}Zr(p,p') and ^{90}Zr(p,n), angle integrated.

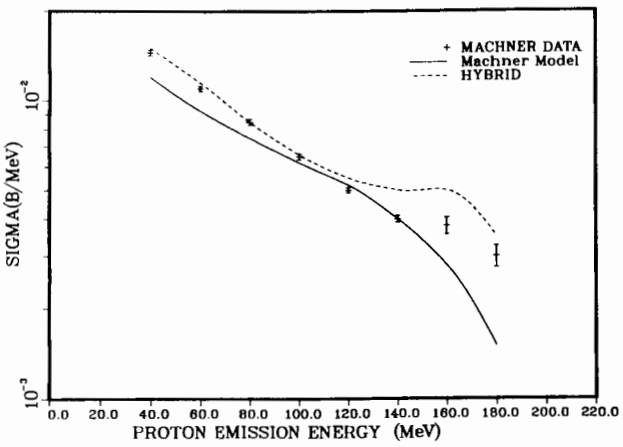

Figure 3: 200 MeV ^{197}Au(p,p'), angle integrated.

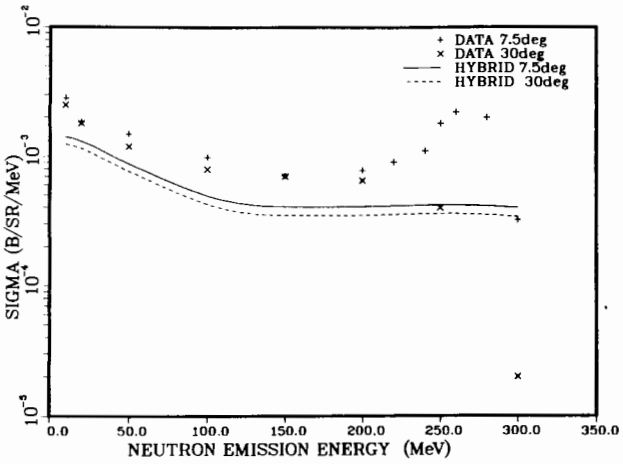

Figure 4: 318 MeV ^{58}Ni(p,n) at 7.5° and 30°.

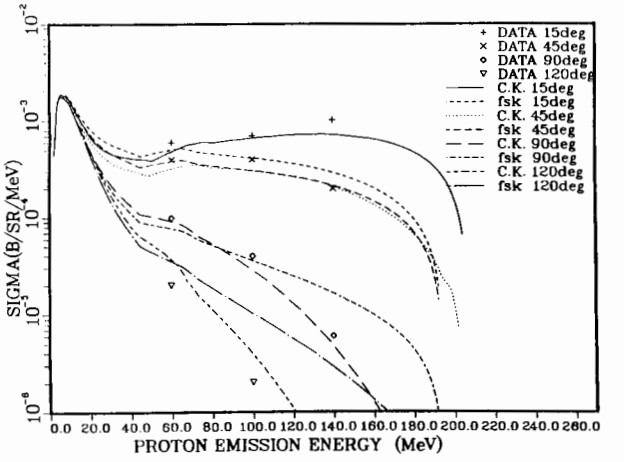

Figure 5: 200 MeV ^{27}Al(p,p') at 15°, 45°, 90°, and 120°.

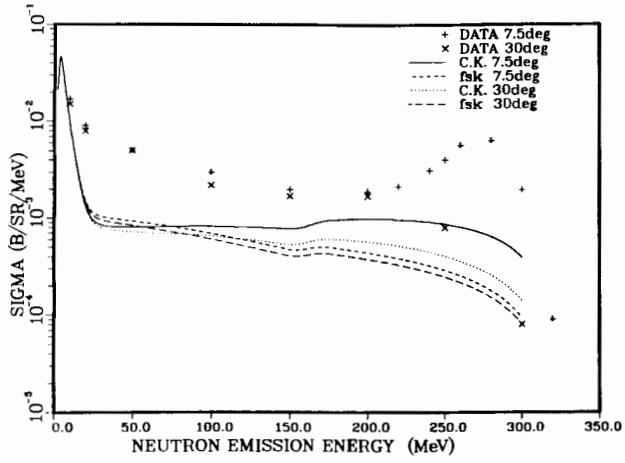

Figure 6: 318 MeV ^{208}Pb(p,n) at 7.5° and 30°.

Eq. (1) model has been benchmarked [10] at incident energies $E \leq 200$ MeV with respect to data and the ALICE code.[7] Figures 1-3 show comparisons at 90 and 200 MeV. A surface model [11] with a hole potential of $\simeq$20 MeV has been implemented in Eq. (1). This hardens the spectra, which is especially evident in Figs. 2 and 3, making this hybrid model comparable to the geometry-dependent hybrid (GDH) model. Figure 4 shows a higher energy case. It is typical of cases in which $E_{incident} \geq 300$ MeV: the hybrid preequilibrium model underpredicts the observed spectra by a factor of two or more. Relaxing the condition of $n \rightarrow 3n$ chaining would improve the low-energy spectra somewhat, but would have little impact at intermediate to high emission energies. However, a more severe constraint is the saturation of the product of depletion factors $\mathcal{D}(n)$ to the value of 1 after a two or more exciton generations,[10] thus contributions from higher exciton states are disallowed.

The GNASH Code

The GNASH exciton-type preequilibrium code [12] has recently been augmented with higher-energy improvements including the nuclear surface model, level density formula, multistage preequilibrium, and both phenomenological and theoretical angular-distributed spectra models.[13] Figures 5 and 6 show comparisons to data at 200 and 318 MeV. Again, for $E_{incident} \geq 300$ MeV, GNASH underpredicts the spectra.

Both preequilibrium models, hybrid and exciton, do not model the quasi-elastic region, which is clearly evident in the forward-angle data ($\theta = 7.5°$) seen in Figs. 4 and 6. Methods for treating various aspects of reactions in this region are discussed in the next section.

The Quasi-elastic Region

The region of quasi-elastic scattering bridges the gap between the low-lying discrete states and the region of compound and pre-equilibrium reactions. The basic reaction mechanism is the single-step quasi-free scattering of the projectile off of a target nucleon. Quasi-elastic scattering therefore offers a useful tool for studying the underlying two-body interaction and its modification by the nuclear medium. It can also be used to study the structure of the nucleus by seeing how it responds to large energy and momentum transfer, as well as to spin and isospin transfer which can be delivered by hadronic probes. Although signatures of shell structure, such as low-lying collective states and giant resonances, disappear at excitation energies above about 20-30 MeV, the nucleus continues to respond collectively in the quasi-elastic region through the residual particle-hole interaction, which has a different character in each spin-isospin channel. This collectivity manifests itself not in sharp states or resonances, but in the gross features of the spectrum, such as shifts in the position and magnitude of the quasi-elastic peak and deviations of the spin observables from the free NN values. Recent experiments at TRIUMF [14,15] and LAMPF [16] have clearly observed these effects in (p,p'), (p,n), and (n,p) reactions near 300 MeV.

In order to get a good theoretical handle on the reaction mechanism and nuclear-structure input required to understand the features of the data, we have investigated several aspects of quasi-elastic projectile-nucleus scattering, which will be briefly outlined in the remainder of this paper. These include 1) the contribution of multi-step processes; 2) the effect of collisional damping of the nuclear response; 3) the "optimal" frame in which to evaluate the two-body amplitudes; and 4) the effect of optical and spin-orbit distortions, which are included in a continuum response calculation using a technique based on the DWIA and the eikonal approximation. These topics are discussed in more detail in Ref. 27.

The Standard Reaction Model

The standard method for calculating quasi-elastic observables assumes that the N-nucleus cross section can be written as a product of the two-body cross section times the nuclear response function

$$\frac{d\sigma}{d\Omega dE} = N_{eff} \sum_{T,S} \frac{k'}{k} tr\{f^{\dagger}_{TS}(\vec{q}) f_{TS}(\vec{q})\} S_{TS}(q,\omega) \qquad (5)$$

where q and ω are the momentum and energy transferred to the nucleus. The sum is over spin (S) and isospin (T) transfer. S_{TS} is the reponse function in the TS channel, and f_{TS} is the corresponding piece of the free NN amplitude. The trace is over both projectile and target nucleon spins. The normalization factor N_{eff} accounts for the attenuation due to the strong absorption. It is the effective number of nucleons seen by the projectile, and is determined in Glauber theory from the in-medium total NN cross section σ

$$N_{eff} = \int d^2b\, T(b)\, e^{-\sigma T(b)} \qquad (6)$$

where the thickness function $T(b)$ is the integral of the nuclear density along the projectile's path at impact parameter b. At intermediate energies σ it is typically 20 to 30 mb, and the reaction is strongly surface-peaked – the main contribution coming from impact parameters where the density is about one-fourth the central value.

If the nuclear response is evaluated in the plane-wave impulse approximation (PWIA) it contains no information that the reaction is surface-peaked. However, this is an important feature which can dramatically alter the response. To include this effect, the slab model was developed by Bertsch, Esbensen, and Scholten.[17] In this model the surface region of the nucleus is approximated as a semi-infinite slab of nuclear matter. The most important ingredient in the model is not the slab wavefunctions, but the use of the surface-peaked probing field

$$\vartheta_q(\vec{r}) = e^{i\vec{q}\cdot\vec{r}} e^{-\sigma T(b)} \qquad (7)$$

in the calculation of $S_{TS}(q,\omega)$. This can be thought of as the product of incoming and outgoing eikonal distorted waves which are evaluated using only the absorptive part of the central optical potential.

The main feature of the slab-model response, in contrast to a plane-wave response, is that it has a long tail in ω. As we will see later, this tail results from the momentum transfer in the distortion, which changes the momentum transfer on the hard collision. Since it includes this important effect, the slab-model is much more successfull in describing quasi-elastic scattering than simpler models based on plane-wave probing fields (such as the Fermi-gas model). Examples of cross sections and spin observables calculated in the slab model can be found in Refs. 15,16,18.

If RPA correlations are included the response is different in each spin-isospin channel. In the $TS = 00$ channel the residual particle-hole interaction is attractive and the strength is pulled down to lower excitation energy, whereas it is pushed to higher energies in the spin and isospin channels where the interaction is repulsive. Thus in charge-exchange reactions the quasi-elastic peak is moved to higher excitation, and in (p,p') the spin observables can deviate substantially from the values based on the free response, since different channels dominate in different regions of ω. Figure 7 shows a sample calculation from Ref. 15 of the analyzing power and spin-flip probability calculated from Eq. (5) using the RPA slab-model response. While the slab-model cannot account for the sharp features seen in the data at low excitation, which are associated with resonances of the finite system, the calculations are nevertheless in reasonably good agreement with the gross features of the data, suggesting that we are indeed seeing the collectivity predicted by the RPA, even at higher excitation energies.

Multi-Step Processes

The standard reaction model can be extended using Glauber theory to include the contribution from multi-step processes in which the projectile has quasi-free collisions with more than one target nucleon. The full cross section can be expressed as a sum over n-step processes [19,20]

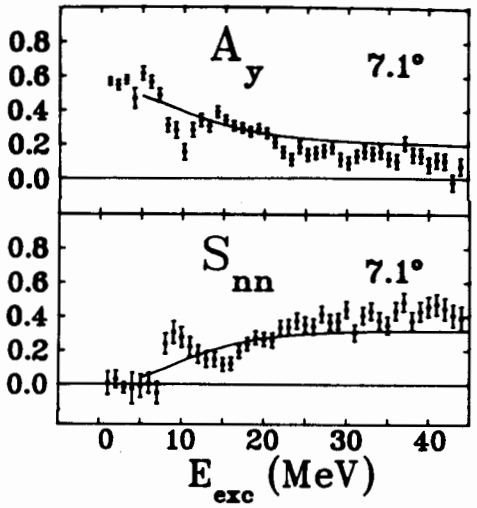

Figure 7: Analyzing power and spin-flip probability for $^{54}Fe(p,p')$ at 290 MeV from Ref. 15.

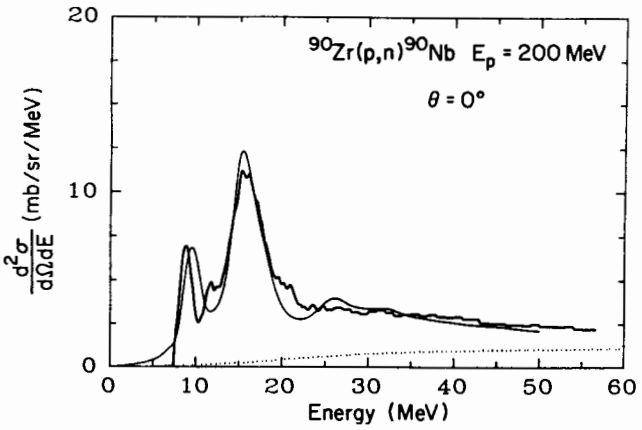

Figure 8: 200 MeV $^{90}Zr(p,n)$ at 0°. The two-step contribution is shown by the dotted line, and the solid line includes both one and two-step contributions. Data is from Ref. 21.

$$\frac{d\sigma}{d\Omega dE} = kk' \sum_{n=1}^{A} D_n(\sigma) W_n(q,\omega) \qquad (8)$$

W_n describes the sequence of n hard collisions, which is essentially a convolution of n two-body cross sections and n one-step response functions. The distortion factor D_n accounts for absorption on the remaining $A-n$ nucleons, and, like N_{eff}, depends on the in-medium NN cross section σ (in fact $D_1 = N_{eff}$). Fortunately, the series in Eq. (8) converges rapidly: successive terms are smaller by roughly an order of magnitude in the region of the quasi-elastic peak [19] so it is usually sufficient to keep only the first two terms. Sample calculations which include two-step contributions can be found in Refs. 16,19,20. In (p,p') reactions the two-step contribution is typically only ~5% of the single-step at the quasi-elastic peak, although it eventually dominates the one-step at higher excitation energies. In (p,n) and (n,p) reactions the two-step can be somewhat larger relative to the one-step, because there are two orderings of charge and non-charge-exchange collisions, and because the non-charge-exchange collision involves the larger isoscalar part of the NN interaction. Furthermore, it can be larger at lower incident energies (say around 200 MeV), because Pauli blocking is more effective in reducing the in-medium NN cross section, which decreases the absorption and increases the two-step relative to the one-step cross section. Figure 8 shows the 0° $^{90}Zr(p,n)$ cross section at 200 MeV. The dotted line shows the two-step contribution and the solid line is the sum of one and two-step contributions. Data are from Ref. 21. In this case the one-step response was evaluated in a full finite-nucleus calculation based on the Second RPA formalism [22] which includes the effect of 2p-2h damping. The two-step was calculated using the slab-model response functions. The slab response does not contain shell structure, which gives rise to the two peaks below ~20 Mev in the one-step calculation, but it should be adequate for the two-step, since any detailed structure will be washed-out by the convolution integrals which yield $W_2(q,\omega)$. Comparing the calculation to the data, we see that the full spectrum out to ~50 MeV is nicely explained by including the two-step. This calculation and its implications for the issue of quenching of Gamow-Teller strength are discussed in more detail in Ref. 20.

2p-2h Damping of the Continuum Response

The response function can be substantially altered at high excitation by the collisional damping of single-particle motion, which corresponds microscopically to the coupling of 1p-1h to 2p-2h or higher configurations. The formalism for including this coupling in full finite-nucleus calculations, known as the Second RPA, has been developed and successfully applied to a variety of reactions.[22] The difficulty is that the method involves very large basis calculations which rapidly become numerically infeasible at large q and ω (for example, even in the giant resonance region there are hundreds of 2p-2h states per MeV in heavy nuclei).

To overcome this problem we have developed an approximate method for including the 2p-2h damping which can easily be applied in regions of high energy and momentum transfer.[23] The basic idea is to replace the microscopic coupling to specific 2p-2h configurations with empirical information already contained in the measured single-particle spreading widths and low-energy phenomenological optical potentials. These are used to construct the self-energies of RPA p-h vibrations which, in a semi-classical limit, depend only on their energy, spin, and isospin. This simplification allows the full response including damping to be expressed as an integral over the RPA response

$$S_{TS}(q,\omega) = \int_0^\infty dE\, S_{TS}^{rpa}(q,E)\, [\rho_{TS}(E,\omega) + \rho_{TS}(E,-\omega)]$$

$$\rho_{TS}(E,\omega) = \frac{\frac{1}{\pi}\Gamma_{TS}(\omega)/2}{[E-\omega-\Delta_{TS}(\omega)]^2 + [\Gamma_{TS}(\omega)/2]^2}$$

$$\Sigma_{TS}(\omega) \equiv \Delta_{TS}(\omega) + i\Gamma_{TS}(\omega)/2 \qquad (9)$$

The Lorentzian function $\rho_{TS}(E,\omega)$ gives the RPA states an energy-dependent shift $\Delta_{TS}(\omega)$ and width $\Gamma_{TS}(\omega)$, which correspond to the real and imaginary parts of the self-energy $\Sigma_{TS}(\omega)$ of states with energy ω, spin S and isospin T. Given the RPA response function, Eq. (9) provides a simple method for including the effect of collisional damping once Σ_{TS} has been determined.

As shown in Ref. 23, the width $\Gamma_{TS}(\omega)$ can be accurately estimated from the empirically determined widths of single-particle and single-hole states $\gamma_h(\omega)$ and $\gamma_p(\omega)$

$$\Gamma_{TS} = \frac{1}{\omega}\int_0^{\omega} d\varepsilon\,[\gamma_p(\varepsilon) + \gamma_h(\varepsilon-\omega)]\,\xi_{TS} \qquad (10)$$

The full width is simply a classical average width for the particles plus holes, multiplied by a factor ξ_{TS} which arises from the quantum coherence of particle and hole decay amplitudes. In the semi-classical model, ξ_{TS} is zero in the $TS = 00$ channel due to a cancellation between single-particle self-energy diagrams and diagrams coming from the interference between particle and hole decay amplitudes. In the spin-isospin channels ($TS \neq 00$), on the other hand, the interference diagrams are themselves small so $\xi_{TS} \approx 1$ and the full width is roughly the average of particle and hole widths.

To complete the evaluation of Σ_{TS}, it remains only to specify how the particle and hole widths γ_p and γ_h are determined empirically. Above the Fermi sea the single-particle widths can be deduced from matrix elements of the absorptive part of the low-energy optical potential, and below the Fermi sea they are determined from the measured spreading widths of hole states. Empirical data for these quantities have been compiled for medium-heavy nuclei by Mahaux and Ngô.[24] The results are reasonably well described by the continuous parameterization

$$\gamma(\varepsilon) = 21.5\left(\frac{\varepsilon^2}{\varepsilon^2+18^2}\right)\left(\frac{110^2}{\varepsilon^2+110^2}\right)\ \text{MeV} \qquad (11)$$

which is assumed to be symmetric about the Fermi energy, so that $\gamma(\varepsilon) = \gamma_p(\varepsilon) = \gamma_h(-\varepsilon)$. Using this parameterization, the the full width can be calculated from Eq. (10), and the real self-energy can be obtained from the imaginary part using a dispersion relation.

Now that Σ_{TS} has been determined, we can return to Eq. (9) and calculate the effect of 2p-2h damping on the slab-model RPA response functions. There is no damping in the $TS = 00$ channel, but in the $TS \neq 00$ channels the response is quenched at the peak and enhanced at higher excitation energies. The effect of damping should therefore be large in charge-exchange and spin-flip reactions, but small in (p,p') which is dominated by isoscalar non-spin excitations.

Figure 9 shows cross sections, calculated using the slab response and Eqs. (5,9-11), for the 300 MeV ^{54}Fe(n,p) reaction along with data at 5°, 8°, and 12° from Ref. 14. The RPA (dashed) and RPA+2p-2h (solid) curves also include the contribution from double scattering. Comparing the solid and dashed curves, we see that the effect of 2p-2h damping is to bring the 1p-1h RPA calculations into nice agreement with both the magnitude and overall shape of the experimental spectra. The magnitude is governed primarily by N_{eff}, which should be fairly accurately determined since it also yields the correct normalization for the (p,p') cross sections at 290 MeV.

It should be emphasized that, although these calculations use the slab response, the method can be applied to any RPA response function. Recently, Co' *et al.* [25] used it to estimate the effect of 2p-2h damping on the (e,e') charge response in ^{12}C and ^{40}Ca, which was treated in a full finite-nucleus continuum RPA. They found that the discrepancy previously observed between theory and experiment can be explained by a combination of the the 2p-2h damping and an effect due to the mean field non-locality.

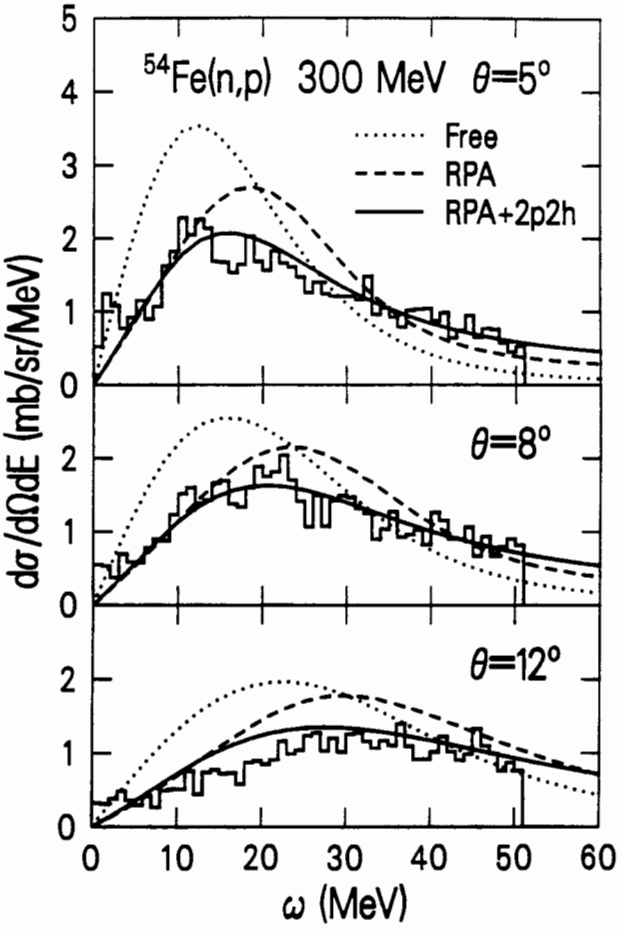

Figure 9: Charge-exchange cross sections compared to experimental data from Ref. 14.

Optimal Frame for Two-Body Amplitudes

So far we have dealt with questions related to the nuclear structure. It is also important to correctly treat the reaction mechanism. In this section we turn to the question of how to evaluate the two-body amplitudes which describe a quasi-elastic collision. In the impulse approximation they are associated with the free on-shell amplitudes derived from experimental phase shifts. Eq. (5) presumes that the NN amplitudes depend only on the incident energy and the momentum transfer $\vec{q}$, but in general they also depend on the momentum of the struck nucleon, which varies due to its Fermi motion. In order to calculate quasi-elastic cross sections it is necessary to integrate over the struck nucleon's Fermi momentum. This problem is greatly simplified if the two-body amplitudes are factored out of the integration by evaluating them in a frame where the struck nucleon's momentum has a constant "optimal" value. Such an approximation is clearly required in order to derive a formula with the factorized structure of Eq. (5). The question of how best to choose this frame has been answered in the non-relativistic theory by Gurvitz and collaborators.[26] The result depends on both momentum transfer and excitation energy. In the case of elastic scattering ($\omega = 0$) the best choice is the Breit frame, in which the struck nucleon has momentum $\vec{p} = -\vec{q}/2$. At the quasi-elastic peak ($\omega = q^2/2m$), the struck nucleon is on average at rest, and the optimal frame is the two-body laboratory frame where $\vec{p} = 0$. In the general case (arbitrary ω), the struck nucleon's momentum is determined by requiring that it satisfies energy conservation: $\omega = (\vec{p}+\vec{q})^2/2m - p^2/2m$, and that it lies along the only preferred direction: that of the momentum transfer $\vec{q}$. Then the optimal momentum is given by

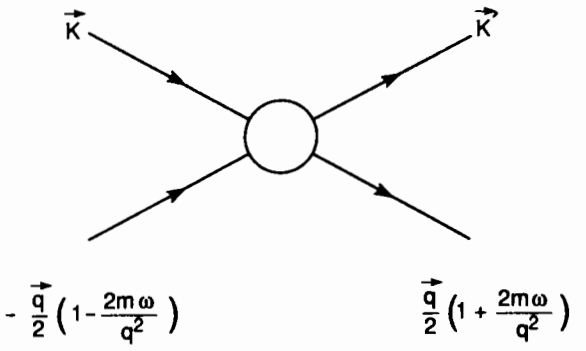

Figure 10: The optimal frame with nonrelativistic kinematics.

$$\vec{p}_{opt} = -\frac{\vec{q}}{2}\left(1-\frac{2m\omega}{q^2}\right) \qquad (nonrelativistic)$$

$$\vec{p}_{opt} = -\frac{\vec{q}}{2}\left(1-\frac{\omega}{q}\sqrt{1+\frac{4m^2}{q^2-\omega^2}}\right) \qquad (relativistic) \quad (12)$$

The second line gives the result using relativistic kinematics. Note that $\vec{p}_{opt}$ reduces to zero at the quasi-elastic peak and to the Breit-frame momentum at $\omega = 0$. A diagram of the optimal frame kinematics is shown in Fig. 10.

Since the experimentally determined amplitudes are usually given in the center-of-mass (c.m.) frame, it is necessary to perform a Lorentz boost to the optimal frame. The method for performing this boost is described in Ref. 27, and involves extracting the invariant Dirac amplitudes from the c.m. amplitudes and then sandwiching them between Dirac spinors in the optimal frame.

The two-body cross section in the optimal frame is expressed in terms of the optimal amplitudes by

$$\frac{d\sigma}{d\Omega_{opt}} = J_{opt}\ tr\{f^{\dagger}_{opt} f_{opt}\} \qquad (13)$$

where J_{opt} is the Jacobian for the transformation between c.m. and optimal frame variables.

Perhaps the most important aspect of the optimal frame is that the invariant energy s varies rapidly with ω due to its dependence on $\vec{p}_{opt}$, and it can be quite different from the energy in the two-body laboratory frame. This can be seen by examining the effective laboratory kinetic energy defined by

$$T_L^{eff} \equiv (s-4m^2)/2m = \frac{E_1E_2 - \vec{k}\cdot\vec{p}_{opt} - m^2}{m} \qquad (14)$$

which can vary by more than $\sim \pm 100$ MeV over the region of the plane-wave response. Such variation will clearly have a large effect on the amplitudes in regions where they are strongly energy dependent.

To illustrate this point, and to show how well the optimal factorization works, consider π-nucleus scattering in the region of the Δ_{33} resonance, where the πN amplitudes vary rapidly

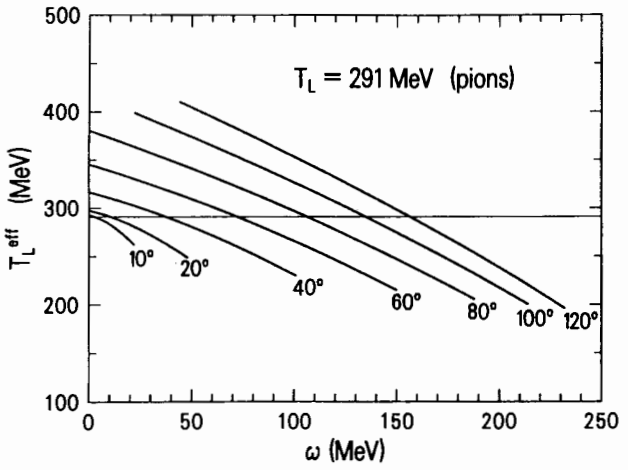

Figure 11: The effective laboratory kinetic energy in the optimal frame for pions incident at 291 MeV.

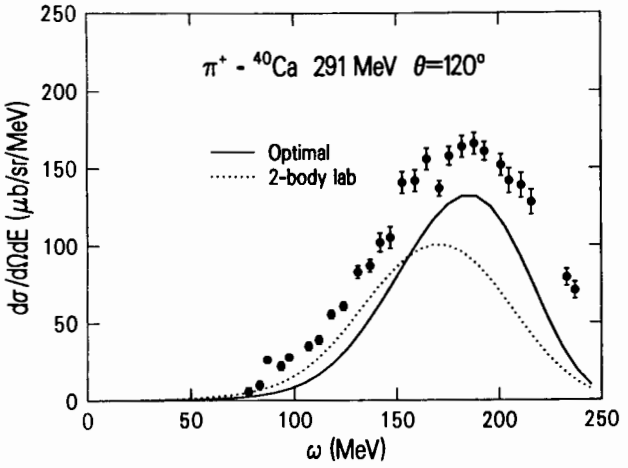

Figure 12: Slab-model calculations with optimal and two-body-lab πN amplitudes compared to data from Ref. 28.

with energy. Figure 11 shows the effective laboratory kinetic energy in the optimal frame for 291 MeV pions scattered at various angles and plotted in the region where the plane-wave Fermi-gas response is nonvanishing. At the large angles we see a variation in T_L^{eff} of more than 200 MeV over the allowed regions of ω. Figure 12 shows cross sections for the 291 MeV $\pi^+ - ^{40}$Ca reaction at 120° using the slab response function and the optimal and two-body-lab amplitudes. Data are from Ref. 28. We see that the optimal calculation agrees well with both the position and magnitude of the peak, while the two-body-lab calculation fails in both respects. At high ω the optimal curve is above the two-body lab curve, because as ω increases, T_L^{eff} decreases, and the πN cross section rises at it nears the peak if the Δ_{33} resonance. The optimal frame also provides a very good approximation to a full calculation where the two-body amplitudes are inside the integration over the nucleon's Fermi momentum.[27] In intermediate energy N-nucleus scattering T_L^{eff} also varies substantially with ω, but the effects are smaller since the NN amplitudes are more slowly varying with energy.

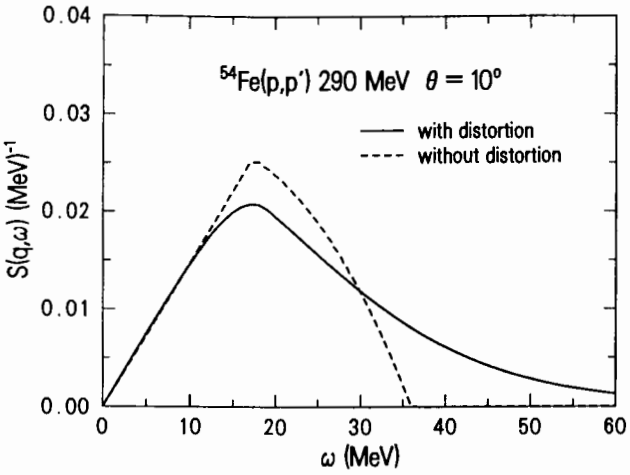

Figure 13: Surface response function calculated from Eq. (15). The dashed line is the plane-wave Fermi-gas response. In the tail region above ~36 MeV the momentum transfer on the hard collision is always greater than the external momentum transfer $\vec{q}$.

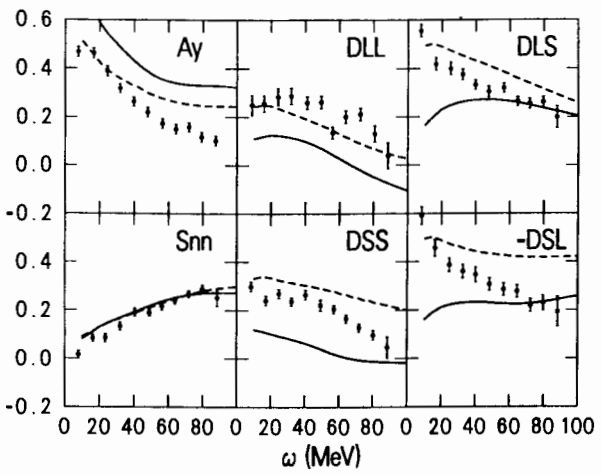

Figure 14: Spin observables with and without the relativistic m^* effect compared to recent data from TRIUMF [33] for 290 MeV ^{54}Fe(p,p') at 20°. Solid curves use $m^* = m$, and dashed curves use $m^* = 0.85m$.

Distorted-Wave Response Calculation

To date, most calculations of the continuum response based on the PWIA or DWIA have used either the c.m. amplitudes, the two-body-lab amplitudes, or the Breit-frame amplitudes. However, these choices violate energy conservation at the two-body level and cannot be consistently applied at arbitrary energy transfers. Even with the optimal amplitudes, the standard reaction model breaks down at large excitation energies beyond the region of the plane-wave response. In this region, if all the momentum transfer occurs on the hard collision then the optimal momentum must be greater than the Fermi-momentum k_F in order to satisfy energy conservation. The way out of this problem is to explicitly include the momentum transfer in the distortion, which changes the momentum transferred on the hard collision, and thereby permits scattering at high ω without violating energy conservation.

Distortion can be included in a relatively simple model based on the DWIA and the eikonal approximation. In Ref. 27 such a model was presented in which the probing field included the full spin-dependent (eikonal) distorted waves as well as the optimal-frame amplitudes. The full response in this model is expressed in terms of a convolution integral with the plane-wave response R_{PW}

$$S(q,\omega) = \int \frac{d^2q'_\perp}{(2\pi)^2} R_{PW}(\vec{q}-\vec{q}'_\perp,\omega)\ |\Delta(\vec{q}'_\perp) f_{opt}(\vec{q}-\vec{q}'_\perp)|^2$$

$$\Delta(\vec{q}'_\perp) = \int d^2b\ e^{i\vec{q}'_\perp\cdot\vec{b}}\, e^{iS(\vec{b})}\, T^{\frac{1}{2}}(b) \qquad (15)$$

where $\vec{q}'_\perp$ is the momentum transferred in the distortion. This expression is slightly more complicated if the spin and isospin dependence are included, in which case Δ becomes a matrix and f_{opt} a vector in the space of projectile spin matrices. $S(\vec{b})$ is the eikonal phase which involves the central and spin-orbit optical potentials. The main new ingredients not present in the standard model of Eq. (5) are the optimal frame NN amplitudes and the use of the full optical potential in the distorted waves. Furthermore, the optimal amplitudes are now inside the integration over $\vec{q}'_\perp$, and are evaluated at the same momentum transfer as the plane-wave response. This insures that the optimal momentum is always less than the Fermi momentum, even at high ω.

The simplest version of the standard model (Eq. 5) can be recovered from Eq. (15) by using only the central absorptive term in the optical potential and factoring f_{opt} and R_{PW} out of the integral by evaluating them at the external momentum transfer $\vec{q}$. A less severe approximation is to only factor f_{opt} out of the integral and leave R_{PW} inside. Then we obtain a surface response function similar to the slab-model response. Figure 13 shows a calculation of the free response with and without distortion based on Eq. (15) with $f_{opt} \to 1$. We have used the Fermi-gas response, $R_{PW} \to R_{FG}$, and normalized by dividing by N_{eff}. In both curves R_{FG} is evaluated at approximately one-third nuclear matter density. The main feature of this calculation is that the distortion produces a long tail in ω which is not present in the plane-wave response. The reason for this is clear from Eq. (15): the convolution integral spreads the plane-wave response over many values of $\vec{q}$. The same effect is responsible for the tail in the slab-model response. An important consequence is that in the region where the plane-wave response vanishes, there is no contribution to the integral if $|\vec{q} - \vec{q}'_\perp| < |\vec{q}|$, because R_{FG} continues to vanish at smaller momentum transfers. Therefore, in the tail region the momentum transfer on the hard collision is always *greater* than the external momentum transfer. This can have a large effect on the observables if the two-body amplitudes vary rapidly with increasing $\vec{q}$.

Figure 14 shows calculations for the 290 MeV ^{54}Fe(p,p') reaction at 20° along with data for the complete set of spin observables which were recently measured at TRIUMF. These calculations include the full spin-dependent distortion and the effect of RPA correlations, which are included by using the interacting Fermi-gas model to evaluate the plane-wave response. We therefore refer to this as the distorted-wave Fermi-gas model (DWFG). The residual interactions are essentially the same as those used in the slab model.[17,27] Note that the ω-dependence of the observables is fairly well predicted by the combination of optimal amplitudes and RPA response functions. Dotted lines show results which incorporate modifications of the NN amplitudes due to the relativistic effective mass m^*, as proposed by Horowitz and Iqbal.[29] The optimal amplitudes were evaluated by sandwiching the invariant Dirac

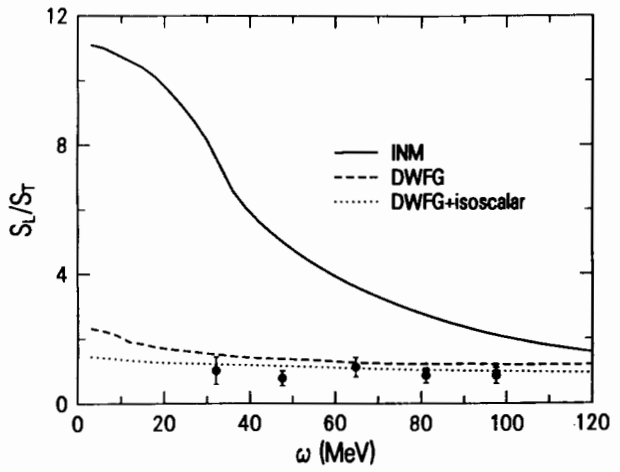

Figure 15: Ratio of longitudinal to transverse isovector spin response along with data from Ref. 32. The solid line is the infinite nuclear matter result, and the dashed and dotted lines are calculated in the distorted-wave Fermi-gas model as described in the text.

amplitudes between spinors with mass $m^* = 0.85m$. This effect does not lead to improved agreement in every case, but it at least moves the curves in the right direction.

In Figure 15 the DWFG model is used to calculate the ratio of longitudinal to transverse isovector spin response, which has been a subject of some controversy in the last few years. Theoretical models based on $\pi + \rho$ exchange predict that at moderate momentum transfers the residual interaction should be substantially different in the longitudinal $(\sigma \cdot \vec{q})$ and transverse $(\sigma \times \vec{q})$ channels.[30] In our calculations we use the same residual interaction as given in Refs. 30,31. Furthermore we include in the Fermi-gas response ΔN^{-1} as well as NN^{-1} excitations as described in these references. As seen in Fig. 15, the longitudinal response can be 2-10 times as large as the transverse response in infinite nuclear matter. However, as seen by the dotted and dashed lines in Fig 15, the difference is completely washed out by the distortion. This effect is mainly due to the absorptive potential in the distortion, although the other effects in Eq. (15) also help reduce the ratio.

The numerical results shown here have for simplicity employed either the slab or the Fermi-gas model for the nuclear structure. It should be emphasized, however, that the techniques are general and can be used with more sophisticated structure input if desired. In particular, the method for including 2p-2h damping based on Eqs. (9-11), and the distorted-wave model of the continuum response in Eq. (15) can be applied to any version of the plane-wave RPA response. One need only calculate the plane-wave response on a grid in q or ω, and then perform the necessary convolution integral, as in Eq. (9) or (15). It is also easy to merge the 2p-2h damping and distorted-wave effects into one calculation by applying the damping integral to the response R_{TS} before inserting it into the distortion integral. When these effects are combined, the result is a simple yet comprehensive model for continuum scattering, which includes the spin-dependent distortion of the projectile, and the effects of RPA correlations and collisional damping which describe the struck nucleon's final state interaction.

References

1. M. Bozoian, E. D. Arthur, R. T. Perry, W. B. Wilson, and P. G. Young, *Calculated Neutron Activation Cross Sections for $E_n \leq 100$ MeV for a Range of Accelerator Materials*, this conference proceedings.
2. E. D. Arthur, P. G. Young, R. T. Perry, D. G. Madland, R. E. McFarlane, R. C. Little, M. Bozoian, and R. J. La Bauve, *Development and Benchmarking of Higher Energy Neutron Transport Data Libraries*, this conference proceedings.
3. M. Blann, Phys. Rev. Lett. **27** (1971) 337.
4. A. Nadasen *et al.*, Phys. Rev. **C23** (1981) 1023.
5. T. E. Ericson, Adv. Phys. **9** (1960) 425.
6. J. M. Akkermans, Phys. Lett. **B82** (1979) 20.
7. M. Blann and H. K. Vonach, Phys. Rev **C28** (1983) 1475.
8. M. Bozoian, *Applied Nuclear Science Research and Development Progress Report, Dec. 1, 1985 - June 30, 1986*, LA-10915-PR.
9. J. Bisplinghoff, Phys. Rev. **C33** (1986) 1569.
10. M. Bozoian, *Applied Nuclear Science Research and Development Progress Report, July 1, 1986 - July 1, 1987*, in preparation.
11. E. Betak and J. Dobes, Z. Phys. **A279** (1976) 319.
12. P. G. Young and E. D. Arthur, *GNASH: A Preequilibrium Statistical Nuclear-Model Code for Calculation of Cross Sections and Emission Spectra*, LANL Report LA-6947 (November 1977).
13. E. D. Arthur and C. Kalbach, Applied Nuclear Science Research and Development Progress Report, Dec. 1, 1985 - June 30, 1986; C. Kalbach, *Systematics of Continuum Angular Distributions: Extentions to Higher Energies*, LANL Report LA-UR-87-4139 (October 1987); M. Bozoian, *A Review of Phenomenological Models for Angular Distributions and Their Comparision with Generalized Preequilibrium Models Incorporating a Free Scattering Kernel*, LANL Report LA-UR-88-337 (February 1988).
14. M. C. Vetterli, *et al.*, Phys. ReV. Lett. **59** (1987) 439.
15. O. Häusser, Can. J. Phys. **65** (1987) 691.
16. C. Glashausser, *et al.*, Phys. Rev. Lett. **58** (1987) 2404.
17. H. Esbensen and G. F. Bertsch, Ann. Phys. **157** (1984) 255.
18. H. Esbensen and G. F. Bertsch, Phys. Rev. **C34** (1986) 1419.
19. R. D. Smith and S. J. Wallace, Phys. Rev. **C32** (1985) 1654.
20. R. D. Smith and J. Wambach, Phys. Rev. **C36** (1987) 2704.
21. C. Gaarde, *et al.*, Nucl. Phys. **A365** (1981) 258.
22. S. Drożdż, V. Klempt, J. Speth, J. Wambach, Nucl. Phys. **A451** (1986) 11.
23. R. D. Smith, J. Wambach, Phys. Rev. **C** (to be published).
24. C. Mahaux, H. Ngô, Phys. Lett. **B100** (1981) 285.
25. G. Co', K. F. Quader, R. D. Smith, J. Wambach, University of Illinois preprint.
26. S. A. Gurvitz, Phys. Rev. **C33** (1986) 422.
27. R. D. Smith *Nucleon-Nucleus Scattering to the Continuum*, Proceedings of the International Conference on Spin Observables of Nuclear Probes, March 13-17, 1988 in Telluride, Colorado (to be published by Plenum Press).
28. G. R. Burleson, *et al.*, Phys. Rev. **C21** (1980) 1452.
29. C. J. Horowitz and M. J. Iqbal, Phys. Rev. **C33** (1986) 2059.
30. W. M. Alberico, M. Ericson, A. Molinari, Nucl. Phys. **A379** (1982) 429.
31. H. Esbensen, H. Toki, G. F. Bertsch, Phys. Rev. **C31** (1985) 1816.
32. T. A. Carey, *et al.*, Phys. Rev. Lett. **53** (1984) 144.
33. O. Häusser, *et al.*, submitted to Phys. Rev. Lett.